Multiresolution Detection of Persistent Scatterers: A Performance Comparison Between Multilook GLRT and CAESAR

Simona Verde, Antonio Pauciullo, Diego Reale, *Member, IEEE,*
and Gianfranco Fornaro, *Fellow, IEEE*

Abstract—Persistent scatterers (PS) interferometry tools are extensively used for the monitoring of slow, long-term ground deformation. High spatial resolution is typically required in urban areas to cope with the variability of the signal, whereas in rural regions, multilook shall be implemented to improve the coverage of monitored areas. Along this line, SqueeSAR and later Component extrAction and sElection SAR (CAESAR) were introduced for the monitoring of both persistent and (decorrelating) distributed scatterers (DS). Multilook generalized likelihood ratio test (MGLRT) is a detector derived in the context of tomographic SAR processing that has been investigated for a fixed multilook degree. In this work, we address MGLRT and CAESAR in the multiresolution context characterized by a spatially variable multilook degree. We compare the two schemes for the multiresolution selection of PS and DS, highlighting the pros and cons of each scheme, particularly the peculiarities of CAESAR that have important implications at the implementation stage. A performance analysis of both detectors in case of model mismatch is also addressed. Experiments carried out with data acquired by the COSMO-SkyMed constellation support both the theoretical argumentation and the results achieved by resorting to Monte Carlo simulations.

Index Terms—Detection, generalized likelihood ratio test (GLRT), persistent scatterers (PS), SAR tomography.

I. INTRODUCTION

METHODS for the coherent, that is interferometric, processing of multitemporal SAR data handle the detection of persistent scatterers (PS) via the measurement of the degree of correlation between the (complex) data stack and a proper parametric model, so to extract reliable information from the estimated parameters [1], [2]. The latter, typically consists of the elevation (or height) associated with the residual topography (RT), the deformation mean velocity (DMV), and seasonal or thermal deformation coefficient [3], [4].

The matching, in the complex domain, to a model presumes the compensation of several disturbing sources (data calibration), especially those directly affecting the phase signal,

as well as of signal components that are not encompassed in the model, such as nonlinear deformations. Beside the noise, additive but also associated with radar echo decorrelation, the atmospheric phase delay/screen (APD/S) introduces in fact a spatially correlated error source, which is of nontrivial compensation in the interferometric processing chain.

The available literature reports two main classes of processing algorithms [5] referred to as persistent scatterer interferometry (PSI) and stacking of coherent interferograms (SCI). Beside the different strategies for interferometric coupling, a key difference between the two classes is related to the use of the multilook operation. The former, with the PSInSAR [1], [6] that was actually pioneer of the development of multitemporal interferometry, operates at full resolution and is particularly suitable for the monitoring of the built environment. The latter, proposed after PSI [7], [8] and originated from a previous work, published later in [9], makes extensive use of the multilook to improve the monitoring capabilities in areas characterized by the presence of weaker (distributed) scattering [7], such as rural zones.

On the wave of the development of tomographic processing for the analysis of the vertical distribution of the backscattering from natural scenes [10], PSI processing for urban areas monitoring has been extended by tomographic methods. Differently from PSI, which exploits only the phase information, tomographic method uses the whole complex measurement and performs a multidimensional imaging [11]–[13]. The tomographic-based PS selection [14] has been framed in the context of radar detection involving the generalized likelihood ratio test (GLRT) [15]. The GLRT detector assumes the probability of false alarm (PFA) as a design feature, which must be controlled, and aims to improve, according to maximum likelihood (ML) estimation criteria, the probability of detection (PD). Beside the capability of detecting also possible PS interfering in the same SAR image pixel, even for classical (single) PS detection, the GLRT approach has shown better detection performances for a fixed PFA [15]–[17].

Regardless of the class to which any algorithm belongs, PSI or SCI, the processing approaches may be roughly schematized in a sequential scheme comprising two main steps. The first step, carried out either with or without the use of multilook, aims at estimating the low spatial-frequencies signal components, mainly the APD and a small-scale (typically at low

resolution) deformation signal. Such estimates are used for the phase calibration of the data, which are then fed to the second step involving an analysis at high-spatial frequencies, generally carried out at full or close-to-full resolution. This second step allows hence "zooming" the scale of analysis for a more detailed (large-scale) monitoring.

Recently, the multilook operation has been further investigated as an operation that allows advanced statistical interferometric SAR data processing that can be implemented at both stages of low- and high-spatial frequency analysis. In the line of the PSI processing, SqueeSAR was proposed as a method able to perform the monitoring of rural areas [18], which are characterized by the presence of typically weak and decorrelating scattering mechanisms, that is distributed scatterers (DS). SqueeSAR performs the DS monitoring via the ML estimation of the phase of an "equivalent" PS (ePS). More specifically, assuming the classical zero-mean Gaussian data distribution, the sample data covariance matrix of the interferometric acquisitions is first estimated through a spatial multiresolution multilook. By extracting the phase of the ePS, SqueeSAR [18] performs a (multibaseline) data filtering that leads to a general improvement of the quality of the interferograms, and, eventually, of the monitored point density. This multibaseline filtering is implemented in [18] since the early stage of the low-frequency analysis in the interferometric processing chain, prior any phase calibration. Both PS and ePS identified by SqueeSAR on the (registered, i.e., spatially aligned) stack of interferometric images follow then the classical PS processing chain. Being, hence, SqueeSAR implemented before the data calibration, no investigations have been carried out from the PS/ePS detection point of view, neither with respect to the PFA, nor for the specific effects of the multilook on the PFA and PD.

The idea of SqueeSAR has been later revisited in the context of SAR Tomography. An approach named CAESAR, i.e., Component extrAction and sElection SAR [19], allows operating a decomposition of the covariance matrix into orthogonal (uncorrelated) components: the components, once sorted into decreasing magnitude order, allow isolating the principal component/components in the measured data. The singular value decomposition (SVD) is in this case exploited: CAESAR performs, therefore, the ePS extraction in the context of principal component analysis (PCA) widely used in many other research areas. Similar to SqueeSAR, CAESAR can be exploited to perform the filtering of the interferometric stack since the stage of low-spatial frequency processing for the APD and small-scale deformation estimation [19]. CAESAR has been applied as well as at the stage of large-scale analysis, after the APD calibration, to operate a detection (CAESAR-D), via the above mentioned GLRT for PS detection, so to trade off the spatial resolution and the density of monitored areas at close-to-full resolution [20]. On one hand, SqueeSAR has the advantage with respect to CAESAR to perform, in principle, an optimal, in the ML sense, estimation of the multibaseline interferometric phase signal. On the other hand, with respect to SqueeSAR, CAESAR does not require the implementation of specific iterative optimizations. This feature applies also to the estimator proposed in [21], which combines the advantages

of both techniques. However, it is worth to point out that iterative operations could be anyway hidden in all the available eigenvector-based tools, somewhere in the linear algebra library. Another peculiar advantage of CAESAR is that it can cope with the presence of multiple interfering components, as those associated with the layover phenomena affecting targets with vertical development (f.i., buildings) [19], [20]. Interference separation/cancellation can improve the small-scale [22], as well as the large-scale analysis in urbanized areas [11].

Finally, still in the framework of SAR Tomography, a multilook GLRT (MGLRT) [23] approach, based on the use of the sample covariance matrix, has been introduced and studied for the detection and monitoring of weak scattering at close-to-full resolution. In this case, the detection approach is somehow complementary: instead of extracting an ePS, which is treated with a detector tailored to a (single-look) PS, the multilook detection scheme (for weak scatterers) acts by reducing the PFA with respect to the single-look case (for a given testing threshold), or equivalently by increasing the PD for a fixed PFA.

The above description provides a summary of the "implicit or explicit" detection steps implemented in the available interferometric processing algorithms. While at full resolution comparison of specific detection schemes, including the method of PSInSAR can be found in the literature [15], open questions still exist for the comparison of multilook detectors, as well as for the selection of the multilook degree and for the flexibility with respect to a possible adaptive choice of the number of exploited pixel.

In this work, we perform a comparison of the MGLRT and CAESAR-D, multilook-based detection of PS/ePS, that allows highlighting the advantages and disadvantages of each of the two approaches. We limit the analysis to single, i.e., noninterfering scattering, thus neglecting the case of possible interference of scattering mechanisms located at different heights [16], because of the interest in increasing the capabilities of monitoring of rural areas.

We specifically focus on the study and comparison of the detection performances of CAESAR-D and MGLRT. This study encompasses the analysis of the PFA and PD as a function of the number of looks. A main contribution is the (analytical) demonstration that CAESAR-D has a PFA independent of the number of looks and equal to the one of single-look GLRT (SGLRT). This feature has important implication from the application point of view, especially in the case of implementation, as of main interest in this work, of a spatially adaptive multilook detection of PS/ePS, characterized by a constant (over the image) PFA level. We resort to the Monte Carlo method to compare the detection performances of CAESAR-D and MGLRT under the same PFA level. A strategy for the implementation of MGLRT, which is known to have PFA curves depending on the number of exploited looks [23], is therefore derived to compare the two detectors also on real data. The two detectors are in this way compared in terms of detection performances, so to highlight the favorable aspects of CAESAR-D related to the independence of the PFA curves from the multilook degree. The analysis highlights for the first time, the problems related to the control of PFA, the possible

This article has been accepted for inclusion in a future issue of this journal. Content is final as presented, with the exception of pagination.

VERDE *et al.*: MULTIRESOLUTION DETECTION OF PS: PERFORMANCE COMPARISON BETWEEN MGLRT AND CAESAR 3

solution, and the available choices for the exploitation of adaptive multilook in multiresolution PS/ePS detection.

The work is organized as follows. Section II describes the GLRT and CAESAR-based multilook detection, Section III analyzes the detection performances on simulated data via the Monte Carlo method. Section IV presents the results of the application of the two detection schemes to data collected by the COSMO-SkyMed sensors to corroborate the theoretical findings and the outcomes of the Monte Carlo simulation. Section V analyzes the behavior of both detectors in the presence of model mismatches, with a particular emphasis to the presence of residual (uncompensated) atmospheric contributions, including a performance analysis on simulated data. Conclusions are then drawn in Section VI.

II. MULTILOOK DETECTION FOR SINGLE SCATTERERS

Let us consider a stack of N range-azimuth focused SAR images, coregistered with respect to a given (master) image. For each range-azimuth pixel, the vector collecting the N images is assumed to be a realization of a complex zero-mean circular Gaussian random vector, whose covariance matrix C in the absence (hypothesis $\mathcal{H}_0$) and the presence (hypothesis $\mathcal{H}_1$) of a single, possibly decorrelating, scatterer is given by

$$C = \sigma_w^2 I_N \tag{1}$$

and

$$C = a(p)a^H(p) \odot \left(\Gamma + \sigma_w^2 I_N \right) \tag{2}$$

respectively, being $\odot$ and $(\cdot)^H$ the Hadamard (elementwise) matrix product and the conjugate and transpose operator. In (1) and (2), $a(p)$ is the unit norm (i.e., $\|a(p)\| = 1$) steering vector, whose nth component is given by

$$\{a(p)\}_n = \frac{1}{\sqrt{N}} \exp\left(-j2\pi \zeta_n^T p\right) \tag{3}$$

$(\cdot)^T$ being the transpose operator, where p is the unknown *parameter vector*, that is the scatterer position in the space spanned by the elevation direction (related to the RT) in the 3-D imaging (tomography), along with the DMV (4-D imaging) and possible seasonal/thermal deformation coefficient (5-D imaging) in the differential tomography [11], [24]; ζ_n is the vector collecting the frequencies (Fourier mate variables) associated with the parameters in p. Such frequencies depend on the adopted system parameters, such as the transmitted wavelength, the spatial baseline distribution, the acquisition epochs, possibly the temperatures, and so on [11]. It should be remarked that (3) imposes a structure on the phase signal that relies on the compensation of the APD: this is a standard assumption in the context of detection of PS. Alternative strategies, not requiring APD/S calibration are also viable: this is, for instance, the case of detectors based on the sole exploitation of the eigenvalues of the sample covariance matrix [25]. However, if on one hand they do not require any phase model as in PS detectors, on the other hand the exploitation of the structure in (3) allows generally improving the detection performances thanks to a coherent integration along the acquisitions. Furthermore, Γ is the covariance matrix

of the backscattering distribution (along the antennas) of the target, which accounts for possible sources of decorrelation. Hereafter, to avoid further complications related to variations of correlation properties, we assume that the target is a PS, thus characterized by a backscattering covariance matrix given by

$$\Gamma = \sigma_\gamma^2 \mathbf{1}_N \tag{4}$$

where, with reference to the imaged PS, σ_γ^2 is the variance of the backscattering coefficient and $\mathbf{1}_N$ is the all-ones structure matrix [26]. Finally, σ_w^2 is the power spectral density (PSD) of the unavoidable noise corrupting the signal and I_N is the $N \times N$ identity matrix.

Multilook schemes for the detection of single PS solve, pixel by pixel, the binary test of hypotheses $\mathcal{H}_0$ versus $\mathcal{H}_1$ by exploiting a set of L (usually less than N) properly selected looks, included the one relevant to the pixel under test. Among them, both MGLRT and CAESAR-D can be analyzed in a common framework by resorting to the sample covariance matrix

$$\widehat{C} = \frac{1}{L} X X^H \tag{5}$$

where $X = [x_1, \ldots, x_L]$ is the $N \times L$ complex data matrix collecting the L processed looks. It is worth noting that the matrix in (5) can be considered a reliable estimate of the statistical covariance matrix of the look associated with the pixel under test if the exploited looks are statistically independent and identically distributed (i.i.d.). More precisely, under the assumed Gaussian distribution, (5) turns out to be the ML estimate of the (statistical) covariance matrix; alternative estimators, able to trade off the accuracy and robustness, may be found in [27]. Finally, in writing the sample covariance matrix as in (5), we are implicitly assuming that, according to the adopted statistical model, the looks are realizations of a zero-mean random process: should this assumption be unrealistic, the subsequent discussion is still valid provided that the covariance matrix is substituted by the correlation matrix.

It is now useful to decompose the matrix in (5) as

$$\widehat{C} = \sum_{k=1}^{\min\{L,N\}} y_k y_k^H \tag{6}$$

where y_k is the kth most powerful component of the processed looks. According to the PCA [28], it is given by

$$y_k = \sqrt{\lambda_k} u_k \tag{7}$$

where λ_k and u_k are the kth highest eigenvalue and the corresponding eigenvector of $\widehat{C}$, respectively.

Detection rules implemented by CAESAR-D and MGLRT can be thus expressed in the unified form

$$\max_{\xi} \frac{\sum_{k=1}^{K} |y_k^H a(\xi)|^2}{\sum_{k=1}^{K} \|y_k\|^2} \underset{\mathcal{H}_0}{\overset{\mathcal{H}_1}{\gtrless}} T \tag{8}$$

where T is a threshold belonging to the interval $(0, 1)$, set according to the desired PFA, and K is the number of involved (principal) components. CAESAR-D is obtained by setting $K = 1$, exploiting just the dominant (most powerful)

component extracted from the looks: in this case (8) specializes to

$$\max_{\xi} \frac{|\boldsymbol{y}_1^H \boldsymbol{a}(\xi)|^2}{\|\boldsymbol{y}_1\|^2} \underset{\mathcal{H}_0}{\overset{\mathcal{H}_1}{\gtrless}} T. \tag{9}$$

MGLRT, instead, assumes $K = \min\{L, N\}$, which, after some trivial algebra handling, allows rewriting (8) as

$$\max_{\xi} \frac{\operatorname{tr}\left[\widehat{\boldsymbol{C}}\boldsymbol{a}(\xi)\boldsymbol{a}^H(\xi)\right]}{\operatorname{tr}\left[\widehat{\boldsymbol{C}}\right]} \underset{\mathcal{H}_0}{\overset{\mathcal{H}_1}{\gtrless}} T \tag{10}$$

thus showing that MGLRT exploits the whole sample covariance matrix.

The detector in (9) was firstly empirically introduced in [25] with a different normalization factor which impacted the false alarms characteristics.

It is worth underlining that MGLRT has been derived according to the well-known tools of the detection theory whereas CAESAR-D stems from empirical considerations [20]. In particular, CAESAR-D applies to the dominant component provided by the PCA (which is in general no more Gaussian distributed), and the same detection rule applied by the SGLRT (i.e., the MGLRT for $L = 1$) to the (Gaussian distributed) data look under testing.

Some summarizing considerations are finally in order.

1) Both MGLRT and CAESAR-D account for the matrix in (5): the first one exploits the whole sample covariance matrix (basically, all the components provided by the PCA); the latter, just its dominant component $\boldsymbol{y}_1$.

2) CAESAR-D decision statistic, for each value of L, is linked to the (non-Gaussian) dominant component $\boldsymbol{y}_1$ through the same functional relationship linking, for $L = 1$ (single-look case), the MGLRT decision statistic to the (Gaussian) look $\boldsymbol{x}$ relevant to the pixel under test. In other words, the (multilook) CAESAR-D can be seen as a two-stage scheme: the first one is a multi-input single-output (MISO) filter, which extracts the dominant component from the data matrix; the second one is the normalized matched-filter, which represents the SGLRT only when the processed data follow the classical Gaussian distribution.

3) In the single-look case ($L = 1$), (9) and (10) became the same decision rule and, thus, CAESAR-D turns out to be the SGLRT scheme.

As for the performances of the analyzed detectors, they are measured by PFA and PD, which are defined as

$$P_{\text{fa}} = P(\mathcal{D}_1|\mathcal{H}_0) \tag{11}$$

and

$$P_d = P(\mathcal{D}_1|\mathcal{H}_1) \tag{12}$$

respectively, being $P(\mathcal{D}_i|\mathcal{H}_j)$ the probability of deciding for the ith hypothesis when the jth is true. Sections III–V are devoted to compare, for a given value of PFA, the PD of MGLRT and CAESAR-D on simulated and real data.
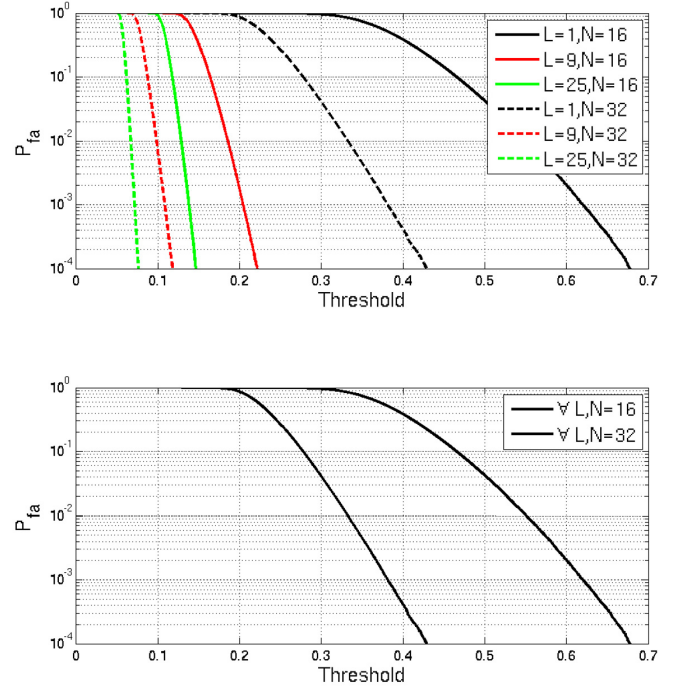

Fig. 1. P_{fa} versus T of (Top) MGLRT and (Bottom) CAESAR-D, for $N = 16$ (solid curves) and $N = 32$ (dashed curves) images and for $L = 1$ (black curves), $L = 9$ (red curves), and $L = 25$ (green curves) looks.

III. PERFORMANCE ASSESSMENT

In this section, we compare the performances of MGLRT and CAESAR-D for the detection of single scatterers in the RT and DMV space (4-D case). The analysis is carried out in terms of PFA and PD, which are evaluated by resorting to Monte Carlo techniques over 10^6 simulated data realizations. Two stacks of $N = 16$ and $N = 32$ images have been generated according to the fluctuating model (see [23, Section IV]). The system parameters are the same of the real X-band data stack of 32 images analyzed in Section IV. In the case $N = 16$, the spatial and temporal baseline distributions have been achieved by distributing uniformly the acquisitions on the spans of the real baselines. We have assumed the presence of a scatterer with parameter vector $\boldsymbol{p} = [0,0]^T$ under $\mathcal{H}_1$. The detectors have been applied to the simulated data sets with three values of L, i.e., $L = 1$, which corresponds to the single-look case, $L = 9$ and $L = 25$. Finally, the RT interval $[-50, 50]$ m and the DMV interval $[-2, 2]$ cm/year have been uniformly sampled with a spacing of 1 m and 0.1 cm/year, respectively.

In Fig. 1, MGLRT and CAESAR-D P_{fa} is plotted versus the detection threshold T with respect to the exploited number of images (N) and looks (L). As expected, both the detectors have a P_{fa} decreasing with T and, for a fixed P_{fa}, a T decreasing with N. Furthermore, the value of T corresponding to a fixed level of P_{fa} is a decreasing function of L for MGLRT, as better highlighted in Fig. 2 where T is plotted versus L for $N = 32$ and $P_{\text{fa}} = 10^{-4}$.

Interestingly, for CAESAR-D P_{fa} results to be invariant with the number of looks and therefore coincident with the one of

This article has been accepted for inclusion in a future issue of this journal. Content is final as presented, with the exception of pagination.

VERDE *et al.*: MULTIRESOLUTION DETECTION OF PS: PERFORMANCE COMPARISON BETWEEN MGLRT AND CAESAR 5
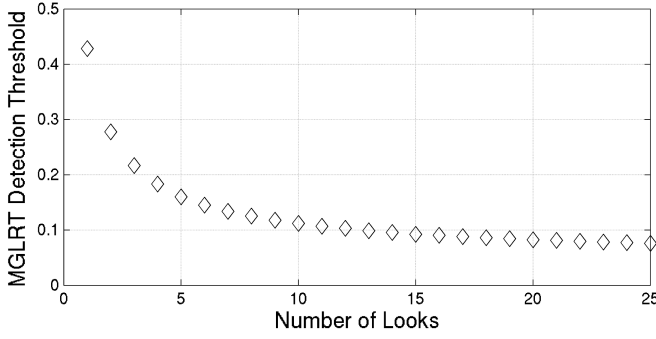
Fig. 2. T versus L of MGLRT detector for $N = 32$ and $P_{\text{fa}} = 10^{-4}$.
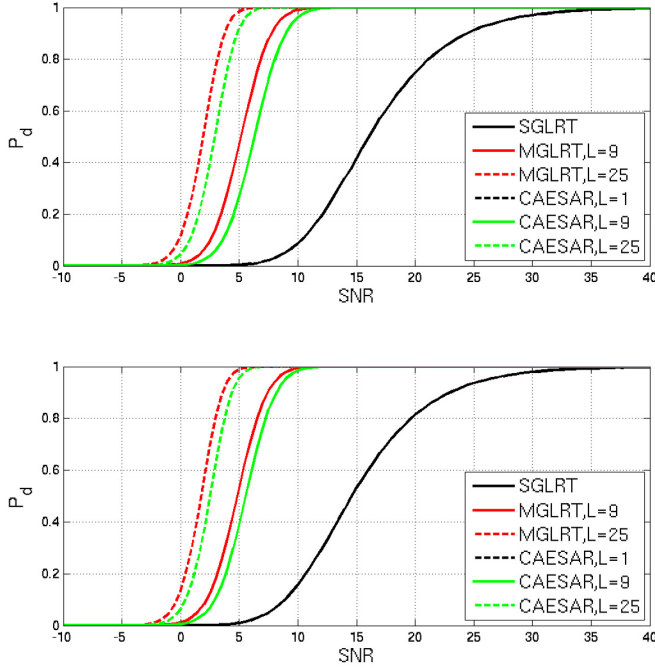

Fig. 3. P_d versus SNR of MGLRT (red curves) and CAESAR-D (green curves), for (Top) $N = 16$ and (Bottom) $N = 32$ images and for $L = 1$ (black curves), $L = 9$ (solid curves), and $L = 25$ (dashed curves) looks.

the SGLRT ($L = 1$). This result, which can be also proved from a theoretical point of view (see Appendix A for some guidelines), has important consequences for the applicability of the detector to real data in the presence of a variable number of looks, as also shown in Section IV. Additionally, it allows to conclude that CAESAR-D, similar to MGLRT, ensures the constant false alarm rate (CFAR) property with respect to the noise level σ_w^2.

Fig. 3 shows the MGLRT and CAESAR-D P_d plotted versus the signal-to-noise ratio (SNR), defined as

$$\text{SNR} = \frac{\sigma_\gamma^2}{\sigma_w^2} \tag{13}$$

for the same values of N and L as in Fig. 1 and for $P_{\text{fa}} = 10^{-4}$. For both detectors, the plots show a gain of P_d associated with an increase in the number of images and/or looks (see [23], Section V-A for a depth description). Moreover, under the same conditions, MGLRT always

performs slightly better than CAESAR-D, although the higher N, the smaller the difference of P_d.

The above analysis has shown two main differences between MGLRT and CAESAR-D:

1) Given a value of P_{fa}, the detection threshold T decreases with the number L of looks for MGLRT, whereas is independent of L for CAESAR-D
2) Given a value of SNR, P_d of MGLRT always overcomes that of CAESAR-D.

In processing real SAR data, point 1) makes the setting of the detection threshold a much more complex issue for MGLRT with respect to CAESAR-D. To better understand this aspect, it is useful noting that both the detectors assume the exploited looks to be i.i.d. However, for real data, the degree of correlation introduced by the acquisition system and classical interferometric SAR processing for data calibration, makes the selected looks, which are typically close to the tested pixel, to be unavoidably statistically dependent. Hence the "effective" number of independent looks, referred to as equivalent number of looks (ENL) and indicated in the following as L_{eq}, is usually lower than L [23]. As a consequence, to properly set the MGLRT detection threshold guaranteeing the desired PFA level, L_{eq} shall be evaluated, which can be not a simple task [29], and exploited in place of L. Additionally, the value of L (and therefore the corresponding L_{eq}) shall be selected pixel-by-pixel to operate multilook of data that are as much as possible homogeneous, thus leading to a multiresolution approach. As a consequence, for MGLRT, the pixel-dependent value of L_{eq} requires the use of pixel-dependent threshold. Contrarily, for CAESAR-D, thanks to the independence of P_{fa} curves from L, neither the evaluation of L_{eq} nor a pixel-dependent setting of the detection threshold is required. This aspect along with the fact that, as highlighted in point 2), MGLRT achieves a gain (although small) of detection performances with respect to CAESAR-D, makes necessary a comparison of the two detectors in terms of both detection capabilities and implementation issues related to the PFA control on real SAR data, which generally involve areas with different characteristics in terms of scattering and noise levels.

IV. RESULTS ON REAL DATA

A performances comparison of MGLRT and CAESAR-D for the detection of single scatterers has been carried out on a real SAR data set composed by 32 images acquired from December 7, 2011 to January 13, 2014 by the COSMO-SkyMed constellation operating in H-Image mode (spatial resolution of $\sim$ 3m) on ascending orbits over the northern surroundings of the city of Naples (South Italy).

The distribution of the acquisitions in the temporal/perpendicular baseline domain is provided in Fig. 4.

The acquisitions have been preliminary phase-calibrated with respect to the contributions associated with the atmospheric propagation and large-scale deformations, which are estimated using the processing algorithm in [30] working at a low resolution, derived from the original small-baseline subset (SBAS) method [7]. In Fig. 5 it is shown the azimuth (vertical)-range (horizontal) map of the DMV corresponding

This article has been accepted for inclusion in a future issue of this journal. Content is final as presented, with the exception of pagination.

6   IEEE TRANSACTIONS ON GEOSCIENCE AND REMOTE SENSING
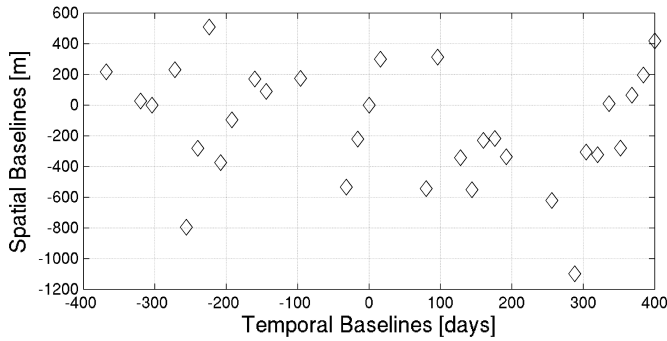

Fig. 4. Distribution of $N = 32$ acquisitions, depicted as diamonds, in the temporal/spatial baseline domain.

to the estimated large-scale deformation, evaluated along the line-of-sight (LOS) oriented toward the sensor and represented in the north-oriented SAR geometry. In this figure the well-known deformation phenomena, reported also in other studies, are well recognizable, that is to say the uplift phenomenon in the Campi Flegrei area [31] close to Naples city and the widespread subsidence phenomenon close to the Volturno estuary [32] in the North-West part of the image. On the top of Fig. 5 a close-up view of the test area investigated in the following, evidenced by a red square, is provided. The area is interested by a landslide approximately moving in East-West direction, as it can be noticed in the close-up view by the slight movement of the ground surface toward the sensor. The top image in Fig. 6 shows the amplitude image of the investigated site at the full spatial resolution achieved by averaging all the available images (multitemporal averaging). It is evident that both rural/sparsely vegetated scenarios as well as a built environment are present.

Multilook detection performances on the real data set have been evaluated by applying the tests in (9) and (10) for two different look selection strategies: plain boxcar and adaptive multilook. First, MGLRT and CAESAR-D detectors have been compared with respect to a fixed-resolution multilook strategy, by considering all the boxcar pixels for two different window sizes. Subsequently, the analysis has involved a multireso-lution multilook strategy based on the adaptive selection of the looks, within the boxcar windows, characterized by a variable number of selected pixels. The latter is based on the use of the Kolmogorov–Smirnov (KS) test [18], [33], which is specifically designed to select a set of neighboring pixels sharing similar amplitude statistical characteristics. This allows exploiting, for each image pixel, only those pixels exhibiting homogeneous amplitude backscattering properties, thus performing an effective adaptive multilook with variable shape and multilook degree. It should be, however, noticed that the KS test is just a possible choice among other amplitude-based adaptive multilooking strategies [34], [35]. As already pointed out in Section III, due to the acquisition system (e.g., data oversampling, intrinsic and/or intentional spectral weighting, interpolation during the coregistration, and so on) adjacent looks turn out to be typically partially correlated even in areas with uncorrelated scattering, such as areas characterized by a fully developed speckle. As a consequence,

setting the detection threshold exploiting L instead of L_{eq} would lead to a level of PFA higher than the desired one, see the top plot in Fig. 1. L_{eq} has been estimated, on each of the amplitude SAR images of the data set, over selected regions characterized by homogeneous scattering located in the half-right portion of the top image in Fig. 6. The estimation has been carried out by varying the number of looks ranging from 2 to 25. The final ENL has been estimated by averaging the results over all the images of the stack. The result is shown in Fig. 7 and highlights that the estimated ENL has almost a linear trend with respect to the number of looks. It is interesting to note the significant reduction of the number of equivalent looks with respect to L for large values of selected looks: this fact reflects in a significant increase of the detection threshold.

In all the experiments, the parameter space spanned by the RT and the DMV has been discretized as in Section III and $P_{fa} = 10^{-4}$ has been set. The map of the detected PSs for the single-look case, which is used as a reference for the subsequent multilook experiments, is reported in the bottom image in Fig. 6. The detection threshold for the assumed P_{fa} is $T = 0.428$, see also the top plot in Fig. 1. The colormap is set according to the estimated component of the residual (with respect to the calibrated large-scale deformation) DMV that, for sake of simplicity, is still referred to as DMV. The colorbar has been halved with respect to the whole DMV span (± 1 cm/year over two years of observation) so to better appreciate the possible presence of outliers typically corresponding to false detections.

A. Boxcar Multilook

The fixed-resolution analysis has been carried out using a boxcar multilook with a 3×3 and 5×5 moving window, resulting in $L = 9$ and $L = 25$ number of looks, respectively.

Concerning the CAESAR-D detector, according to the fact that the PFA is independent of L, a detection threshold corresponding to the one of the single-look case (i.e., $T = 0.428$), has been fixed for both the multilook cases. As for MGLRT detection, according to Fig. 7, $L_{eq} = 4$ and $L_{eq} = 10$ has been set for $L = 9$ and $L = 25$, respectively. The resulting (constant) detection thresholds are $T = 0.183$ and $T = 0.112$, respectively.

The maps of detected ePS for CAESAR-D (top) and MGLRT (bottom) are given in Fig. 8 for the cases $L = 9$ (left column) and $L = 25$ (right column). The increase of the detection performances with respect to the single-look case is evident, but results in a clear spatial resolution loss, especially on urban area textures, see the images in the right column.

A comment on the comparison of MGLRT and CAESAR-D results is in order. The shown maps seem to confirm the capabilities of MGLRT to increase the density of detected scatterers with respect to CAESAR-D. However, the maps, that according to the measured ENL should be characterized by the same P_{fa} level, show as well as an increased number of outliers for the MGLRT case, which become even more evident for the case $L = 25$. Outliers may denote an increase of the "real" P_{fa} level with respect to the one derived by Monte Carlo

This article has been accepted for inclusion in a future issue of this journal. Content is final as presented, with the exception of pagination.

VERDE *et al.*: MULTIRESOLUTION DETECTION OF PS: PERFORMANCE COMPARISON BETWEEN MGLRT AND CAESAR 7
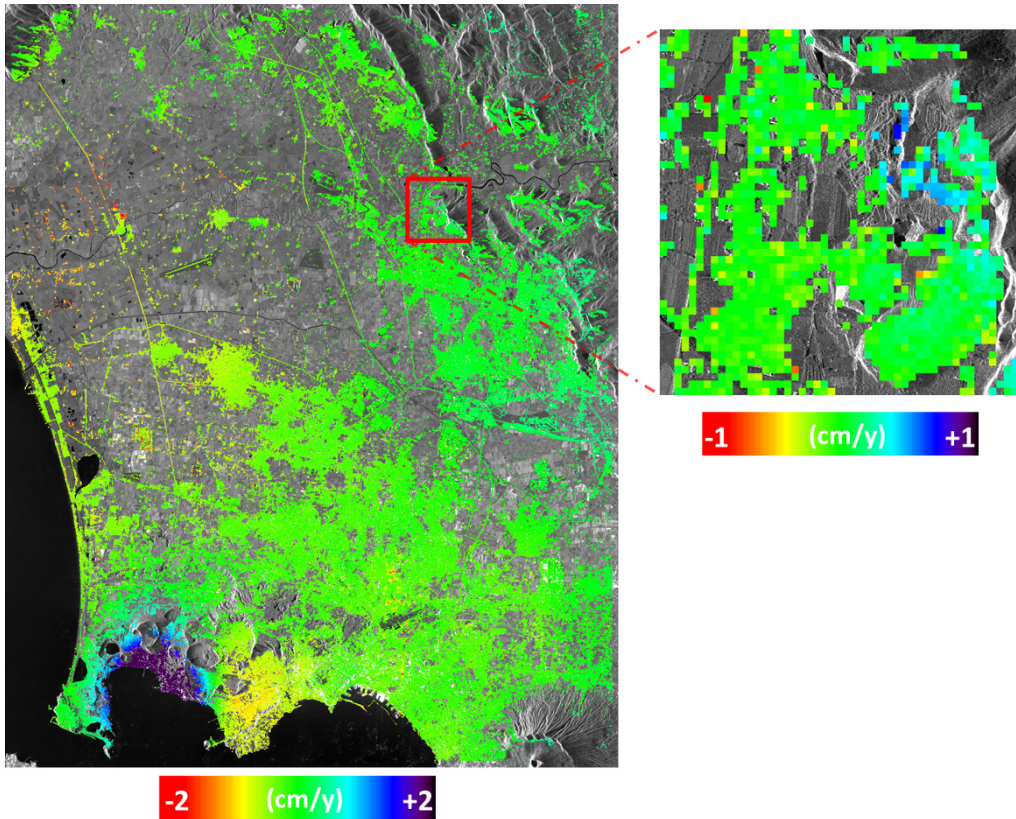

Fig. 5. Map of the LOS DMV on the Naples area and its northern surroundings (South Italy) retrieved downstream of the modified SBAS low-resolution processing in [30]. The red square and corresponding right zoom image highlight the test area for subsequent detection analysis. Colormaps are set according to the estimated DMV.

simulations based on the i.i.d. Gaussian looks assumption. On one hand, no guarantee can be given on the fact that such outliers in the MGLRT maps correspond to false detections, which might be generated by either an inexact setting of the ENL, or by the constraint related to the fixed degree of multilook choice in the presence of (a few) heterogeneous pixels. On the other hand, the CAESAR-D detection maps show the effects, on a real scenario, related to the possibility to select the threshold independently of the number of exploited looks: Outliers on CAESAR-D maps appear to be less than those on MGLRT maps (see top and bottom images in Fig. 8) and compatible with the ones of the single-look case (see Fig. 6).

B. Multiresolution Processing

A multiresolution detection based on the use of the KS test for the selection of statistically homogeneous looks has been analyzed. As already specified previously, for the purpose to compare the results with those achieved with fixed-resolution approach, we again use boxcar windows of 3×3 and 5×5 pixel sizes, but now a search for pixels with similar amplitude statistics is operated within these boxes. Given the aim of retaining the lowest possible value of L in urban areas, the KS test level of significance $\alpha = 60\%$ has been set (further details about the KS test are given in Appendix B). The parameter α allows trading off the preservation of the resolution and the effective degree of multilook.

Fig. 9 reports the map of statistically similar pixels (brothers) identified by the KS test for the two cases of search window size. It can be noticed that, as expected, in areas characterized by the presence of PSs (f.i. urban scenarios) a lower number of brothers is found, whereas in areas characterized by a spatially uniform backscattering, typically exhibiting lower SNR with respect to urban environments and therefore prone to decorrelation phenomena (rural/sparsely vegetated areas), the number of brothers increases.

Fig. 9 clearly conveys the information about the capability of the multiresolution approach to perform an effective multilook, fitting the scattering variability of the imaged scene, that is to allow improvements in the ePS detection capabilities in areas characterized by weak/decorrelating scattering, while preserving the resolution in urban areas.

An important remark about the detection threshold setting for MGLRT is now in order. As highlighted by the performances analysis on simulated data in Section III, given a certain PFA the detection threshold T decreases with the number L of looks. Since the multiresolution approach implies the use a pixel-variant number of looks (brothers), for MGLRT it is necessary to set up a pixel-variant detection threshold depending on the exploited number of looks. Said differently, the use of a multiresolution MGLRT with a constant detection threshold does not allow guaranteeing a constant level of PFA over the scene.

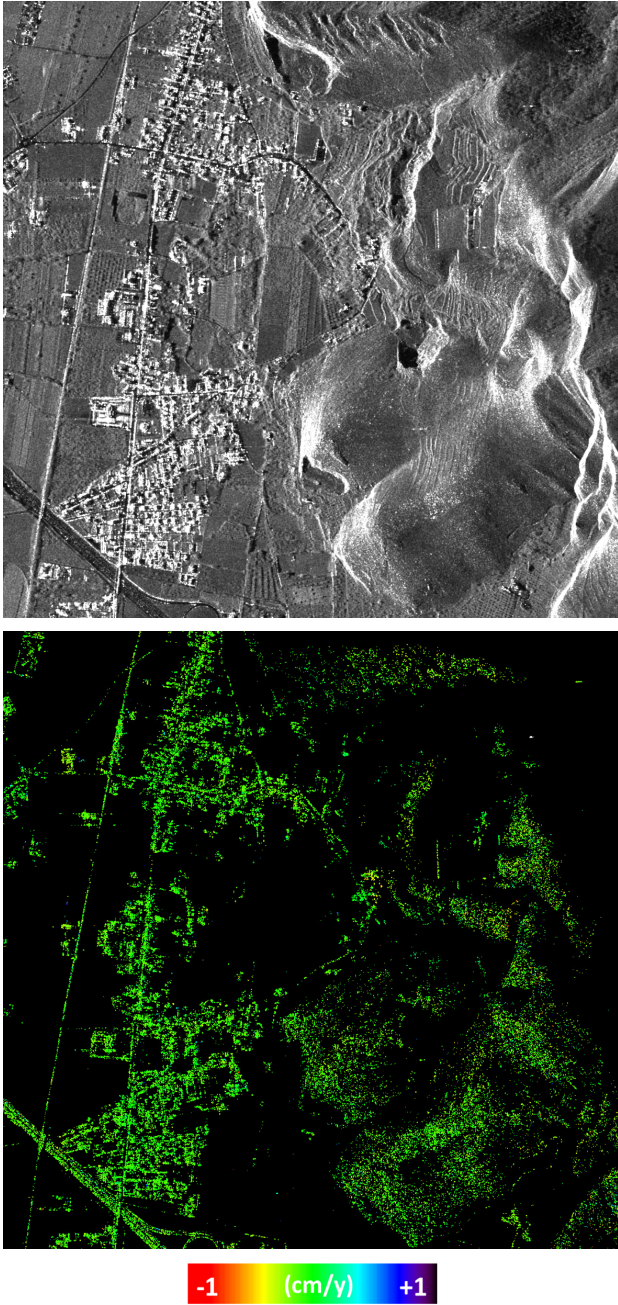Fig. 7.   Estimated ENL for a number of looks L ranging between 1 and 25.

Fig. 6.   (Top) Multi-image amplitude map of the test site (average of 32 CSK images). Vertical and horizontal axis corresponds to azimuth (S-N) and range directions (W-E). (Bottom) Map of the single-look ($L = 1$) detected (single) scatterers. Colormap is set according to the estimated DMV.

from the multiresolution analysis: left and right column are associated with the different size windows corresponding to $L \leq 9$ and $L \leq 25$, respectively.

The experimental results show that both CAESAR-D and MGLRT allow achieving a significant improvement with respect to the single-look, especially in areas characterized by weak/decorrelating scatterers with low SNR suffering for poor P_d values. The multiresolution performs a suitable filtering that preserves the high resolution in urban areas and operates at the same time an effective multilook in rural areas. Moreover, differently from the fixed-resolution multilook detection whose map of detected ePS is shown in Fig. 8, the possibility to reduce the multilook degree allows preserving the resolution almost independently of the size of the search window in urban areas. It should be also remarked that operating on the parameter α, that is on the level of significance of the test, it is possible to balance even with an adaptive approach, the degree of resolution with respect to the density of detected PS, to trade off the results between the single look case (see Fig. 6) and the fixed-resolution multilook case (see Fig. 8).

Finally, it is worth to note that a comparable detection behavior of MGLRT and CAESAR-D is achieved in a multiresolution context. However MGLRT processing requires a pixel-dependent detection threshold able to guarantee the desired PFA on the whole scene. To better highlight the consequences of a fixed threshold choice for the multiresolution MGLRT case, Fig. 11 reports the map of detected scatterers achieved by adaptively selecting the set of brothers (whose cardinality is shown in the right image in Fig. 9) and exploiting for the MGLRT test a fixed threshold for the whole image. More precisely, the threshold has been set to a value corresponding to $L_{eq} = 2$ providing almost the same number of detected pixels as for the variable threshold multiresolution MGLRT shown in the bottom right part of Fig. 10. To highlight the increase of the level of outliers, a zoomed-in view of the selected area is shown for both fixed and variable threshold processing. The comparison shows rather clearly that, for a given number of detected ePS, the choice of a constant threshold for MGLRT provides a higher level of outliers.

Hence, to preserve the same level of P_{fa} imposed for the single-look case:

1) for CAESAR-D a constant detection threshold corresponding to the one of the single-look case has been retained;

2) for MGLRT case a pixel-by-pixel detection threshold has been selected according to value of L_{eq} corresponding to the pixel-variable multilook degree, which is intrinsic to the multiresolution approach.

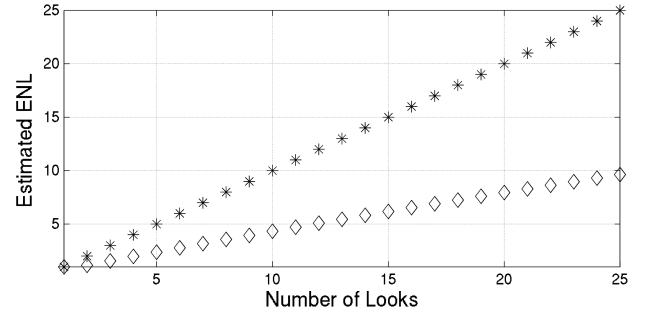Fig. 10 shows the maps of detected ePS for CAESAR-D (top row figures) and MGLRT (bottom row figures) resulting

V. FURTHER DISCUSSIONS ON PERFORMANCE ANALYSIS

Performance analysis has been carried out by assuming the selected looks to be perfectly calibrated, with respect to the phase terms deviating from the assumed structure of the steering vector in (3), and also homogeneous.
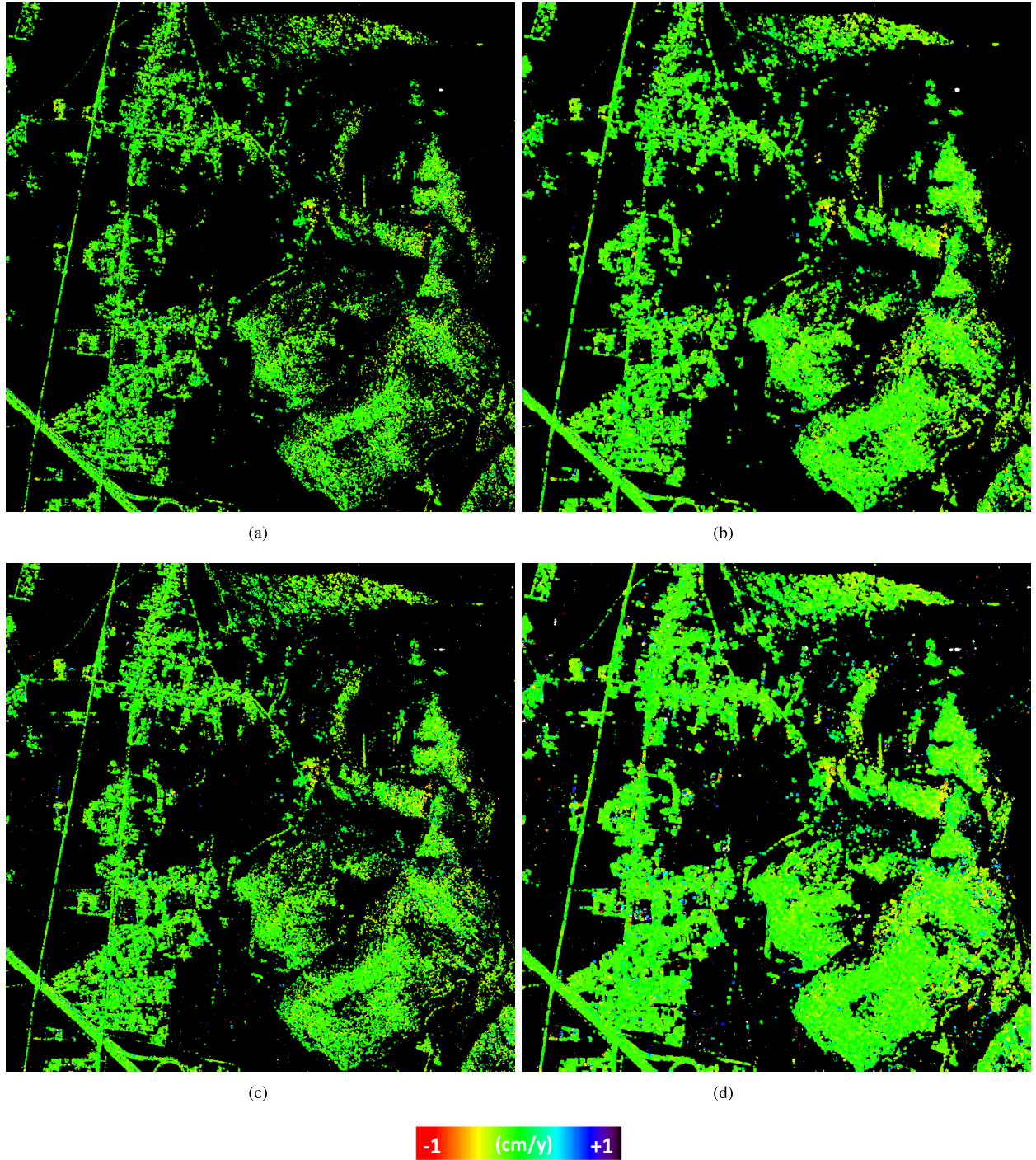
This article has been accepted for inclusion in a future issue of this journal. Content is final as presented, with the exception of pagination.

VERDE *et al.*: MULTIRESOLUTION DETECTION OF PS: PERFORMANCE COMPARISON BETWEEN MGLRT AND CAESAR
9

Fig. 8. Distribution of (a) and (b) CAESAR-D and (c) and (d) MGLRT detected single scatterers for (left) $L = 9$ and (right) $L = 25$. The same level of P_{fa} imposed for the single-look ($L = 1$) case has been preserved. Colormap is set according to the estimated DMV. (a) CAESAR-D ($L = 9$). (b) CAESAR-D ($L = 25$). (c) MGLRT ($L = 9$; $L_{\text{eq}} = 4$). (d) MGLRT ($L = 25$; $L_{\text{eq}} = 10$).

We start by considering the calibration issue and in particular we analyze the effects of the presence of possible residual (i.e., not compensated) APD. The analysis has been carried out by exploiting the same setup as in Section III with reference to $N = 32$ images and for $L = 9$ looks. The residual APD has been simulated by adding an unmodeled phase term to the phase of the PS steering vector. The range delay (measured in cm) associated with the residual APD

has been generated, at each antenna, as a realization of a zero-mean Gaussian random variable, with standard deviation σ_{APD}. Moreover, to account for the spatially low-pass nature of the APD, the same realization has been exploited on each processed look.

Fig. 12 shows the P_d plotted versus the SNR achieved by SGLRT, MGLRT and CAESAR-D for four values of σ_{APD}. The plots highlight for all the detectors a shift toward higher

This article has been accepted for inclusion in a future issue of this journal. Content is final as presented, with the exception of pagination.

10   IEEE TRANSACTIONS ON GEOSCIENCE AND REMOTE SENSING
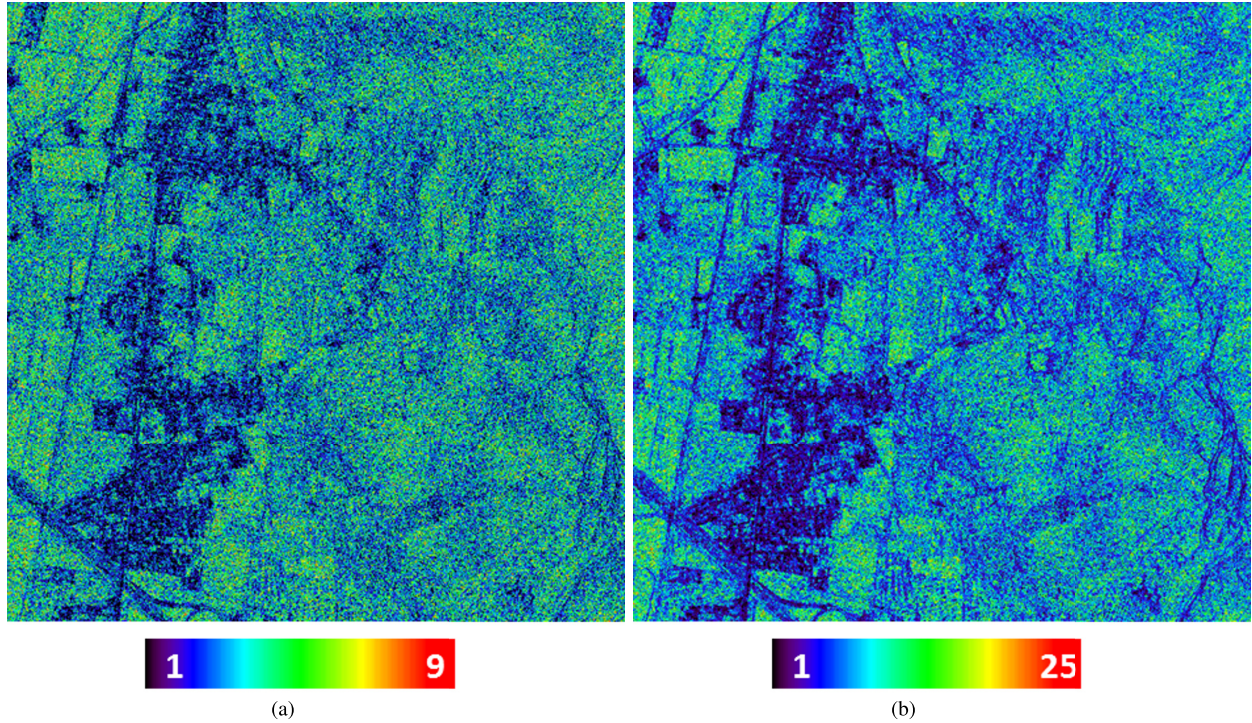

Fig. 9. Map of the number of brothers identified by the KS test. A moving search window of (a) 3×3 and (b) 5×5 pixels has been used, resulting in a maximum number $L = 9$ and $L = 25$ statistically similar pixels, respectively. KS test level of significance $\alpha = 60\%$ has been retained. (a) $L \leq 9$. (b) $L \leq 25$.

values of SNR as the standard deviation of the residual APD increases. Moreover, while the MGLRT is able to reach a $P_d = 1$ also in the presence of residual APD, provided that the SNR is sufficiently high, SGLRT and CAESAR-D have both a maximum value of $P_d < 1$, as small as high is the APD standard deviation.

To better understand such a behavior, it would be interesting to analyze the analytical expressions of the detection rules of both MGLRT and CAESAR-D under $\mathcal{H}_1$ and in the presence of a residual APD. To this aim, we assume that the exploited looks are independent realizations of a complex zero-mean circular Gaussian random vector, whose covariance matrix can be achieved by the one in (2), with $\boldsymbol{\Gamma}$ given by (4), provided that the following substitution is made:

$$a(p) \rightarrow a_\varphi = a(p) \odot a_{\mathrm{APD}}. \tag{14}$$

The unmodeled complex phase-only vector a_{APD} accounts for the residual APD: it randomly changes the structure of the steering vector $a(p)$, leading to the unmodeled unit norm direction a_φ. The sample covariance matrix is thus

$$\widehat{C} = \widehat{\sigma_\gamma^2} a_\varphi a_\varphi^H + \widehat{C}_w + 2\Re\{\widehat{C}_{sw}\} \tag{15}$$

where $\widehat{\sigma_\gamma^2}$ is the sample variance of the PS backscattering coefficient γ, $\widehat{C}_w$ is the sample covariance matrix of the additive noise w, and $\widehat{C}_{sw}$ is the sample mutual correlation between the signal $s = \gamma a(p)$ and noise w. Accordingly, the MGLRT and CAESAR-D detection rules are

$$\frac{\widehat{\sigma_\gamma^2}|a^H a_\varphi|^2 + a^H \hat{N} a}{\mathrm{trace}(\widehat{C})} \underset{\mathcal{H}_0}{\overset{\mathcal{H}_1}{\gtrless}} T(L) \tag{16}$$

and

$$|a^H u_1|^2 \underset{\mathcal{H}_0}{\overset{\mathcal{H}_1}{\gtrless}} T \tag{17}$$

respectively, where, for sake of simplicity, we have denoted by a the steering vector corresponding to the (estimated) vector parameters maximizing the statistic of the tests. In (16), $\hat{N} = \widehat{C}_w + 2\Re\{\widehat{C}_{sw}\}$ accounts for the overall noise effect and the dependence of the detection threshold on the number of looks has been explicitly highlighted. In (17), u_1 is the eigenvector associated with the highest eigenvalue of $\widehat{C}$. The comparison between (16) and (17) provides suggestion on the interpretation of the asymptotic (with SNR) differences in the performances shown in Fig. 12, as well as on the different approach exploited by two detectors in revealing the presence of a PS.

With a finite number L of looks, when SNR $\rightarrow \infty$ the test statistics of both the detectors reduce to $|a^H a_\varphi|^2$, which measures the maximum match between the structured direction $a(p)$ and the unstructured direction a_φ. Such a match can assume even very low values in case of high residual APD, according to its standard deviation. However, while the CAESAR-D has the highest and invariant with L detection threshold (equal to the one of the SGLRT), the MGLRT can lower its threshold by increasing the number of looks. Accordingly, depending on the standard deviation of the APD, the same (low) value of the match can stay always below the CAESAR-D threshold independently of L, while for the MGLRT the match could be above the threshold, thus providing the detection of the scatterer. A remark however is in order. Although the MGLRT can, in principle, achieve the maximum level of P_d, it is also to be noticed that the matching

This article has been accepted for inclusion in a future issue of this journal. Content is final as presented, with the exception of pagination.

VERDE *et al.*: MULTIRESOLUTION DETECTION OF PS: PERFORMANCE COMPARISON BETWEEN MGLRT AND CAESAR   11
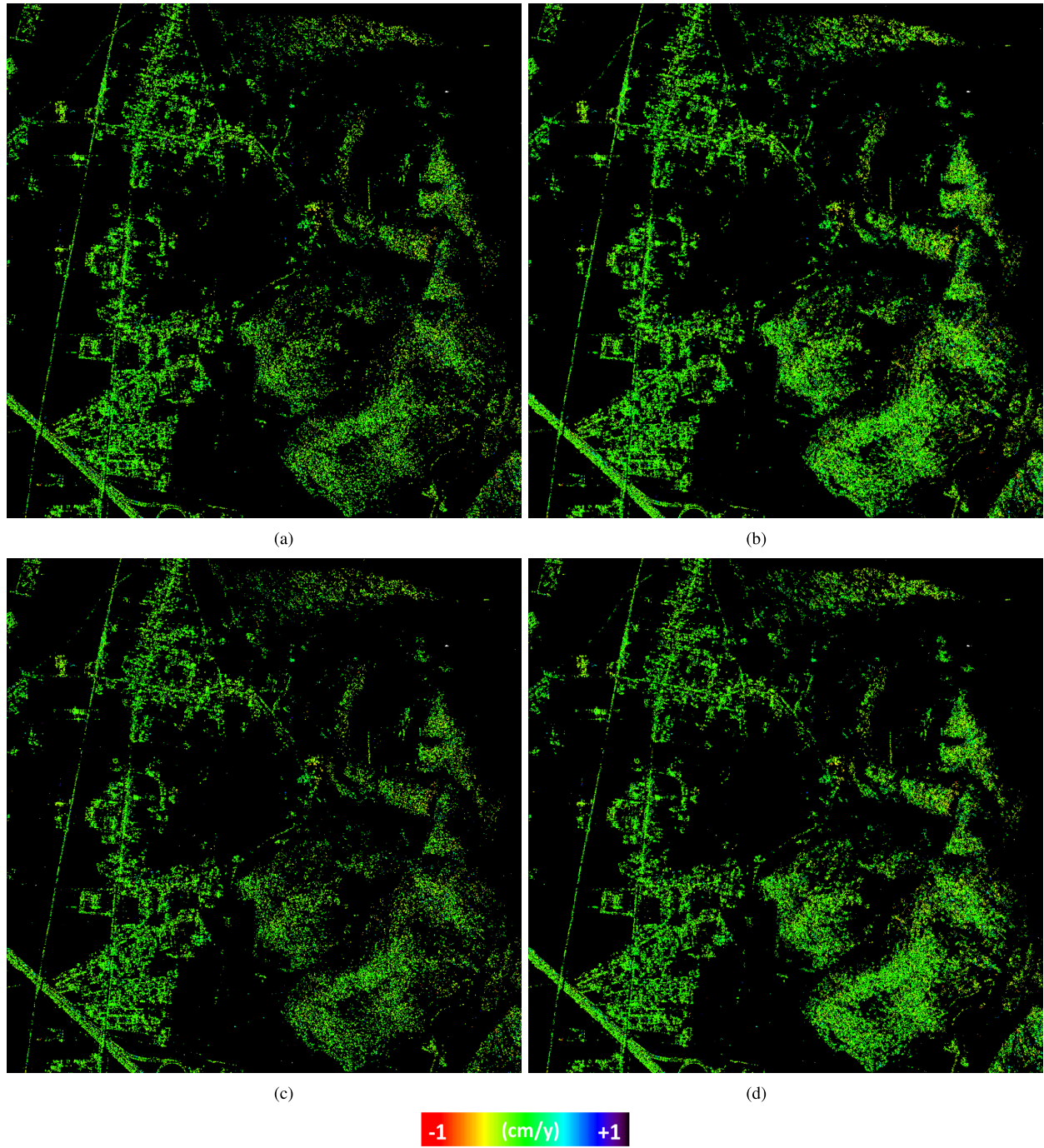

Fig. 10. Distribution of (Top) CAESAR-D and (Bottom) MGLRT detected single scatterers for statistical similar pixels selected by the KS test in (a)–(c) 3×3 and (b)–(d) 5×5 search window. Colormap is set according to the estimated DMV. (a) CAESAR ($L \leq 9$). (b) CAESAR ($L \leq 25$). (c) MGLRT ($L \leq 9$). (d) MGLRT ($L \leq 25$).

between a structured and an unstructured direction leads to the impossibility of estimating the scatterer parameters. In other words, with a high residual APD, a possible present PS can be detected by the MGLRT but cannot be characterized.

The detection approach of the two tests can be more easily understood by analyzing their asymptotic expression with L. The case $L \rightarrow \infty$ obviously provides $\widehat{\sigma_\gamma^2} = \sigma_\gamma^2$, $\widehat{\boldsymbol{C}_n} = \boldsymbol{C_w}$ and $\boldsymbol{u}_1 = \boldsymbol{a}_\varphi$, so that the detection rules for MGLRT and CAESAR-D reduces to

$$\frac{\sigma_\gamma^2 |\boldsymbol{a}^H \boldsymbol{a}_\varphi|^2 + \sigma_w^2}{\sigma_\gamma^2 + N\sigma_w^2} \underset{\mathcal{H}_0}{\overset{\mathcal{H}_1}{\gtrless}} T(\infty) \qquad (18)$$

and

$$|\boldsymbol{a}^H \boldsymbol{a}_\varphi|^2 \underset{\mathcal{H}_0}{\overset{\mathcal{H}_1}{\gtrless}} T \qquad (19)$$

respectively. Both detectors, as in the case SNR $\rightarrow \infty$ discussed above, maximize the scalar product measuring the match between the structured vector $\boldsymbol{a}(\boldsymbol{p})$ and the unstructured vector $\boldsymbol{a}_\varphi$. However, while CAESAR-D analyzes only the scalar product between the steering and, for finite L, the estimate of $\boldsymbol{a}_\varphi$, MGLRT accounts, as evident in (16) and even more in (18), also for the distribution of the power along all the eigenvectors, see the total (estimated or statistical)

This article has been accepted for inclusion in a future issue of this journal. Content is final as presented, with the exception of pagination.

12   IEEE TRANSACTIONS ON GEOSCIENCE AND REMOTE SENSING
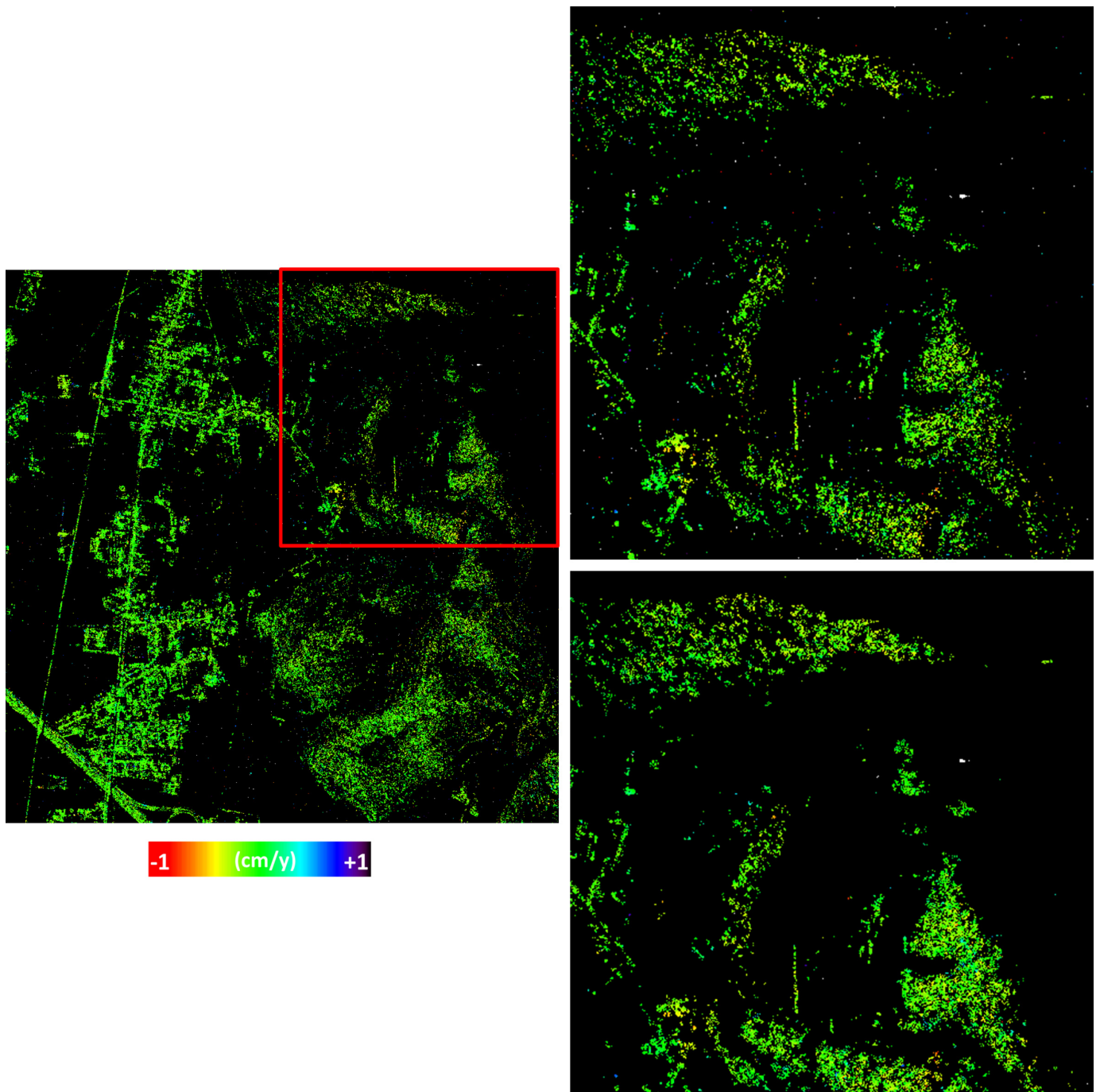

Fig. 11.   (Left) Map of MGLRT detected single scatterers for statistical similar pixels selected by the KS test in 5×5 search window where a constant detection threshold corresponding to $L_{eq} = 2$ has been set. The zoomed-in view of the area highlighted by the red box is reported in the top-right image. The zoom on the same area of the MGLRT detected single scatterers with variable threshold in Fig. 10(d) is reported in the bottom-right image. Colormap is set according to the estimated DMV.

power at the denominator. The presence of direction in which the power is larger than an aliquota of the total power associated with the detection threshold reveals the presence of an (unstructured) PS.

To conclude, whereas the eigenvalues in CAESAR approach can be exploited at the interferogram generation stage [19] (see, f.i, the identification of interfering scatterers over buildings for the generation of "building flattened" interferograms in layover areas, so as to aid also the phase unwrapping (PhU)

procedure [22]), CAESAR-D only tests the structure of the scattering. Conversely MGLRT, which decreases the threshold (up to $1/N$) according to the exploitation of all eigenvalues, is more prone to the detection also of unstructured scattering. While, on one hand, it should be highlighted that a test for the presence of unstructured scatterers by means of the eigenvalues distribution extracted by CAESAR is in principle possible in a separate stage, after the structured detection [25], on the other hand, the choice of the most appropriate multilook

This article has been accepted for inclusion in a future issue of this journal. Content is final as presented, with the exception of pagination.

VERDE *et al.*: MULTIRESOLUTION DETECTION OF PS: PERFORMANCE COMPARISON BETWEEN MGLRT AND CAESAR 13
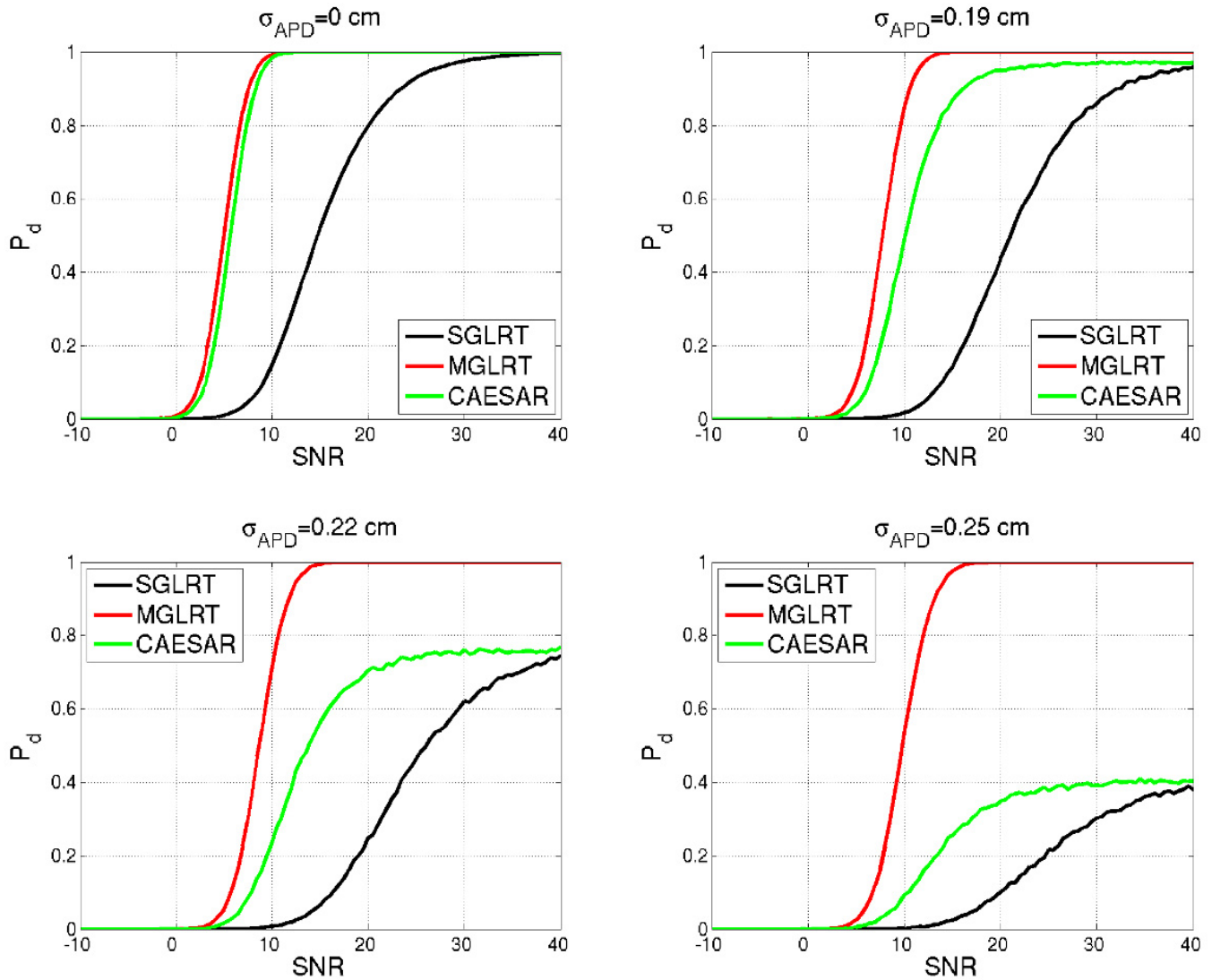

Fig. 12. P_d versus SNR of SGLRT (black curves), MGLRT (red curves) and CAESAR-D (green curves), for $N = 32$ images and $L = 9$ looks. A residual APD affects the phase signal, with a standard deviation of (Top-left) 0 cm, (Top-right) 0.19 cm, (Bottom-left) 0.22 cm, and (Bottom-right) 0.25 cm.

detector should account also for the specific peculiarities of each scheme according to the specific application and to the need to include or avoid the detection of unstructured scatterers for which the parametric information, necessary also for the correct geolocalization, becomes less relevant.

Above analysis and considerations can also guide to figure out the behavior of the detectors in presence of inhomogeneous looks, which may be particularly critical when averaging pixels in areas characterized by highly variable scattering. This can be the case of the presence of height dispersion of scatterers, as f.i. in urban areas where layover can lead to the presence of multiple (generally two or maximum three) components, see the CAESAR based analysis in [20]. Assuming a perfect compensation of the APD, the spilling of the power from the dominant component affects the detection performances of both detectors. Experimental results, not included for brevity, confirm the losses as a translation of the curves toward higher SNR levels with a slight increase of the fork between the

detection curves of CAESAR-D and MGLRT. This behavior can be explained with the fact that the power decrease on the principal component affects the estimation of the scatterer parameters for CAESAR-D [see (17)] whereas for MGLRT the spilling of power in the noise subspace leads to an overestimation of the noise level [see (16)]. This behavior could be one of the reason for which, especially for the case $L = 25$ the points detected by MGLRT in the case of a fixed number of looks is larger than that of CAESAR-D in the urban area in Fig. 8. No saturation phenomena as those pertinent to phase miscalibration case are, however, present. Although better statistically homogeneous pixel selection strategy with respect to KS could be in principle implemented [35]–[37] it should be remarked that this problem has a limited relevance in this work, which is tailored to the analysis of multiresolution detection schemes able to preserve the resolution in zones, as urban areas, characterized by a high spatial variability of the scattering. In these regions the proposed multiresolution

This article has been accepted for inclusion in a future issue of this journal. Content is final as presented, with the exception of pagination.

14   IEEE TRANSACTIONS ON GEOSCIENCE AND REMOTE SENSING

scheme shall implement a small multilook, at the limit it shall use a single look. Stated differently, multilook is here conceived mainly to increase the detection performances in an unbuilt environment. Finally, it is worth noting that situations in which multiple components are expected, as for instance in implementing multilook in urban areas, should be analyzed by detectors tailored to multiple components (see [16] and [17] and [23] and [38] for single and multilook solutions, respectively).

VI. Conclusion

The work has addressed the comparison of two multilook approaches for the detection of ePS introduced in the literature: CAESAR-D and MGLRT. We have shown that, although MGLRT has in principle a gain in the detection performance (under the assumed statistics) with respect to CAESAR-D, the latter, as exploited in this work, is characterized by the advantage of having a PFA that is independent on the number of looks: this feature has important implications from the implementation point of view. In fact, in the (frequent) case of the presence of a scenario involving both urban and rural areas, this allows a straightforward implementation of a detection based on adaptive, variable number of looks able to effectively exploit, on one side, the accuracy and resolution of the full resolution analysis for the spatial localization of the scatterers in built areas, and, on the other side, the capabilities of the multilook operation to improve the performances on the detection and monitoring of weaker scatterers in nonurbanized regions. To guarantee a constant PFA over the image, differently from CAESAR-D, MGLRT is shown to require a much more involved setting of the threshold, spatially variable over the scene to follow the variations of the multilook degree, specifically of the ENL. However, as for the detection performances, even on simulated data generated according to the statistic under which MGLRT has been derived, CAESAR-D achieves comparable detection performances. Tests on real data acquired by the COSMO-SkyMed constellation have been included to verify all aspects investigated in the work from both the theoretical and simulation point of view that is the invariance of the CAESAR-D PFA with respect to the number of looks, as well as the similar detection performances of the two detectors. Differences in the performances of MGLRT and CAESAR-D appear more evident in the presence of model mismatch. A detailed analysis carried out by assuming uncompensated atmospheric disturbances has highlighted the deep differences in the detection performances, stemming from the different strategies in the use of the signal coherence during the detection. CAESAR-D, similar to the SGLRT detector, strongly relies on the model matching, whereas MGLRT allows achieving satisfactory detection performances even in the presence of large mismatch, provided that the SNR is high. Advantages and disadvantages of each detection scheme with respect to the model mismatch depend, however, on the specific use of the detector when applied to the detection of PS.

Appendix A

With reference to a given range-azimuth pixel, let $\boldsymbol{x}$ and $\boldsymbol{y}$ be the single-look and dominant principal component extracted from the corresponding multilook sample covariance matrix, respectively. Moreover, let $\widetilde{\boldsymbol{x}} = \boldsymbol{x}/\|\boldsymbol{x}\|$ and $\widetilde{\boldsymbol{y}} = \boldsymbol{y}/\|\boldsymbol{y}\|$ be their unitary norm transformation.

SGLRT and CAESAR-D allow testing the presence of a single PS within the considered pixel by processing $\widetilde{\boldsymbol{x}}$ and $\widetilde{\boldsymbol{y}}$, respectively, with the same test

$$\max_{\boldsymbol{\xi}}|\widetilde{\boldsymbol{z}}^H \boldsymbol{a}(\boldsymbol{\xi})|^2 \underset{\mathcal{H}_0}{\overset{\mathcal{H}_1}{\gtrless}} T \tag{20}$$

where the unit norm vector $\widetilde{\boldsymbol{z}}$ should be properly specialized for the exploited detector. Accordingly, to prove that SGLRT and CAESAR-D have the same PFA, it is enough to demonstrate that, under the hypothesis $\mathcal{H}_0$, $\widetilde{\boldsymbol{x}}$ and $\widetilde{\boldsymbol{y}}$ have the same probability density function.

To this aim, it is worth noting that, independently of its statistical distribution, a random vector $\boldsymbol{x} \in \mathbb{C}^N$, $\mathbb{C}$ being the complex numbers field, has always a corresponding $\widetilde{\boldsymbol{x}}$ which is a point belonging to the surface of the unit ray hypersphere in $\mathbb{C}^N$, whose statistical distribution depends only on that of the phase of $\boldsymbol{x}$. Accordingly, since under $\mathcal{H}_0$ the look $\boldsymbol{x}$ is distributed as complex circular zero-mean uncorrelated Gaussian random vector and recalling that each its component has phase and modulus which are Uniform (in a 2π length interval) and Rayleigh distributed, respectively, it is straightforward to show that $\widetilde{\boldsymbol{x}}$ is uniformly distributed over the unit ray hypersphere. Moreover, $\widetilde{\boldsymbol{y}}$ is an eigenvector (the one associated with the highest eigenvalue, although this is not relevant for our discussion) of the sample covariance matrix of the exploited looks, which under $\mathcal{H}_0$ is a realization of a Wishart random matrix. In [39] it is shown that all the eigenvectors of such a matrix are uniformly distributed over the unit ray hypersphere, which is the same statistical distribution of $\widetilde{\boldsymbol{x}}$.

Appendix B

With reference to a set of SAR images, let d_1 and d_2 be the random variables associated with the amplitude values of two different looks at the generic acquisition.

The (two-sample) KS test asserts that the looks are drawn from the same statistical distribution if

$$\delta < c \tag{21}$$

where δ is the maximum value of the absolute difference between the empirical cumulative distribution functions (c.d.f) $\hat{F}_{d_1}$ and $\hat{F}_{d_2}$ of d_1 and d_2, respectively, that is

$$\delta = \max_x |\hat{F}_{d_1}(x) - \hat{F}_{d_2}(x)| \tag{22}$$

and c is the threshold corresponding to the desired significance level α. The latter is given by

$$\alpha = 1 - H_\delta(c) \tag{23}$$

where $H_\delta(t)$ is the c.d.f of δ, expressed by the KS distribution [33], [40]–[42]

$$H_\delta(t) = 1 - 2\sum_{n=1}^{\infty}(-1)^{n-1}e^{-2n^2t^2}. \tag{24}$$

It is worth noting that, according to (21) and (23), the higher the significance level α, the lower the threshold c, and,

thus, the lower the probability that the looks under test are considered statistically homogeneous.

REFERENCES

[1] A. Ferretti, C. Prati, and F. Rocca, "Permanent scatterers in SAR interferometry," *IEEE Trans. Geosci. Remote Sens.*, vol. 39, no. 1, pp. 8–20, Jan. 2001.

[2] M. Costantini, S. Falco, F. Malvarosa, and F. Minati, "A new method for identification and analysis of persistent scatterers in series of SAR images," in *Proc. IGARSS IEEE Int. Geosci. Remote Sens. Symp.*, Jul. 2008, pp. II-449–II-452.

[3] X. X. Zhu and R. Bamler, "Let's do the time warp: Multicomponent nonlinear motion estimation in differential SAR tomography," *IEEE Geosci. Remote Sens. Lett.*, vol. 8, no. 4, pp. 735–739, Jul. 2011.

[4] D. Reale, G. Fornaro, and A. Pauciullo, "Extension of 4-D SAR imaging to the monitoring of thermally dilating scatterers," *IEEE Trans. Geosci. Remote Sens.*, vol. 51, no. 12, pp. 5296–5306, Dec. 2013.

[5] M. Crosetto, O. Monserrat, M. Cuevas-González, N. Devanthéry, and B. Crippa, "Persistent scatterer interferometry: A review," *ISPRS J. Photogram. Remote Sens.*, vol. 115, pp. 78–89, May 2016.

[6] A. Ferretti, C. Prati, and F. Rocca, "Nonlinear subsidence rate estimation using permanent scatterers in differential SAR interferometry," *IEEE Trans. Geosci. Remote Sens.*, vol. 38, no. 5, pp. 2202–2212, Sep. 2000.

[7] P. Berardino, G. Fornaro, R. Lanari, and E. Sansosti, "A new algorithm for surface deformation monitoring based on small baseline differential SAR interferograms," *IEEE Trans. Geosci. Remote Sens.*, vol. 40, no. 11, pp. 2375–2383, Nov. 2002.

[8] O. Mora, J. J. Mallorqui, and A. Broquetas, "Linear and nonlinear terrain deformation maps from a reduced set of interferometric SAR images," *IEEE Trans. Geosci. Remote Sens.*, vol. 41, no. 10, pp. 2243–2253, Oct. 2003.

[9] S. Usai, "A least squares database approach for SAR interferometric data," *IEEE Trans. Geosci. Remote Sens.*, vol. 41, no. 4, pp. 753–760, Apr. 2003.

[10] A. Reigber and A. Moreira, "First demonstration of airborne SAR tomography using multibaseline L-band data," *IEEE Trans. Geosci. Remote Sens.*, vol. 38, no. 5, pp. 2142–2152, Sep. 2000.

[11] G. Fornaro, F. Lombardini, A. Pauciullo, D. Reale, and F. Viviani, "Tomographic processing of interferometric SAR data: Developments, applications, and future research perspectives," *IEEE Signal Process. Mag.*, vol. 31, no. 4, pp. 41–50, Jul. 2014.

[12] X. X. Zhu and R. Bamler, "Very high resolution spaceborne SAR tomography in urban environment," *IEEE Trans. Geosci. Remote Sens.*, vol. 48, no. 12, pp. 4296–4308, Dec. 2010.

[13] X. X. Zhu and R. Bamler, "Tomographic SAR inversion by L_1-norm regularization—The compressive sensing approach," *IEEE Trans. Geosci. Remote Sens.*, vol. 48, no. 10, pp. 3839–3846, Oct. 2010.

[14] M. A. Siddique, U. Wegmuller, I. Hajnsek, and O. Frey, "Single-look SAR tomography as an add-on to PSI for improved deformation analysis in urban areas," *IEEE Trans. Geosci. Remote Sens.*, vol. 54, no. 10, pp. 6119–6137, Oct. 2016.

[15] A. De Maio, G. Fornaro, and A. Pauciullo, "Detection of single scatterers in multidimensional SAR imaging," *IEEE Trans. Geosci. Remote Sens.*, vol. 47, no. 7, pp. 2284–2297, Jul. 2009.

[16] A. Pauciullo, D. Reale, A. De Maio, and G. Fornaro, "Detection of double scatterers in SAR tomography," *IEEE Trans. Geosci. Remote Sens.*, vol. 50, no. 9, pp. 3567–3586, Sep. 2012.

[17] A. Budillon and G. Schirinzi, "GLRT based on support estimation for multiple scatterers detection in SAR tomography," *IEEE J. Sel. Topics Appl. Earth Observ. Remote Sens.*, vol. 9, no. 3, pp. 1086–1094, Mar. 2016.

[18] A. Ferretti, A. Fumagalli, F. Novali, C. Prati, F. Rocca, and A. Rucci, "A new algorithm for processing interferometric data-stacks: SqueeSAR," *IEEE Trans. Geosci. Remote Sens.*, vol. 49, no. 9, pp. 3460–3470, Sep. 2011.

[19] G. Fornaro, S. Verde, D. Reale, and A. Pauciullo, "CAESAR: An approach based on covariance matrix decomposition to improve multibaseline–multitemporal interferometric SAR processing," *IEEE Trans. Geosci. Remote Sens.*, vol. 53, no. 4, pp. 2050–2065, Apr. 2015.

[20] G. Fornaro, A. Pauciullo, D. Reale, and S. Verde, "Multilook SAR tomography for 3-D reconstruction and monitoring of single structures applied to COSMO-SKYMED data," *IEEE J. Sel. Topics Appl. Earth Observ. Remote Sens.*, vol. 7, no. 7, pp. 2776–2785, Jul. 2014.

[21] H. Ansari, F. De Zan, and R. Bamler, "Efficient phase estimation for interferogram stacks," *IEEE Trans. Geosci. Remote Sens.*, vol. 56, no. 7, pp. 4109–4125, Jul. 2018.

[22] S. Verde, D. Reale, A. Pauciullo, and G. Fornaro, "Improved small baseline processing by means of CAESAR eigen-interferograms decomposition," *ISPRS J. Photogramm. Remote Sens.*, vol. 139, pp. 1–13, May 2018.

[23] A. Pauciullo, D. Reale, W. Franze, and G. Fornaro, "Multi-look in GLRT-based detection of single and double persistent scatterers," *IEEE Trans. Geosci. Remote Sens.*, vol. 56, no. 9, pp. 5125–5137, Sep. 2018.

[24] F. Lombardini, "Differential tomography: A new framework for SAR interferometry," *IEEE Trans. Geosci. Remote Sens.*, vol. 43, no. 1, pp. 37–44, Jan. 2005.

[25] G. Fornaro, W. Franze, A. Pauciullo, D. Reale, and S. Verde, "Aspects of multilook SAR tomography," in *Proc. IEEE Int. Geosci. Remote Sens. Symp. (IGARSS)*, Jul. 2015, pp. 2923–2926.

[26] A. Pauciullo, A. De Maio, S. Perna, D. Reale, and G. Fornaro, "Detection of partially coherent scatterers in multidimensional SAR tomography: A theoretical study," *IEEE Trans. Geosci. Remote Sens.*, vol. 52, no. 12, pp. 7534–7548, Dec. 2014.

[27] Y. Wang and X. X. Zhu, "Robust estimators for multipass SAR interferometry," *IEEE Trans. Geosci. Remote Sens.*, vol. 54, no. 2, pp. 968–980, Feb. 2016.

[28] I. Jolliffe, *Principal Component Analysis*. Hoboken, NJ, USA: Wiley, 2005, doi: 10.1002/0470013192.bsa501.

[29] S. N. Anfinsen, A. P. Doulgeris, and T. Eltoft, "Estimation of the equivalent number of looks in polarimetric synthetic aperture radar imagery," *IEEE Trans. Geosci. Remote Sens.*, vol. 47, no. 11, pp. 3795–3809, Nov. 2009.

[30] G. Fornaro, A. Pauciullo, and F. Serafino, "Deformation monitoring over large areas with multipass differential SAR interferometry: A new approach based on the use of spatial differences," *Int. J. Remote Sens.*, vol. 30, no. 6, pp. 1455–1478, Mar. 2009.

[31] L. D'Auria *et al.*, "Magma injection beneath the urban area of Naples: A new mechanism for the 2012–2013 volcanic unrest at campi flegrei caldera," *Sci. Rep.*, vol. 5, no. 1, Aug. 2015, Art. no. 13100.

[32] L. Cascini *et al.*, "Detection and monitoring of facilities exposed to subsidence phenomena via past and current generation SAR sensors," *J. Geophys. Eng.*, vol. 10, no. 6, Dec. 2013, Art. no. 064001, doi: 10.1088/1742-2132/10/6/064001.

[33] M. A. Stephens, "Use of the Kolmogorov-Smirnov, Cramér-Von Mises and related statistics without extensive tables," *J. R. Stat. Soc. Ser. B, Methodol.*, vol. 32, no. 1, pp. 115–122, 1970.

[34] A. Parizzi and R. Brcic, "Adaptive InSAR Stack Multilooking Exploiting Amplitude Statistics: A Comparison Between Different Techniques and Practical Results," *IEEE Geosci. Remote Sens. Lett.*, vol. 8, no. 3, pp. 1489–1492, May 2011.

[35] F. Sica, D. Reale, G. Poggi, L. Verdoliva, and G. Fornaro, "Nonlocal adaptive multilooking in SAR multipass differential interferometry," *IEEE J. Sel. Topics Appl. Earth Observ. Remote Sens.*, vol. 8, no. 4, pp. 1727–1742, Apr. 2015.

[36] Y. Wang, X. X. Zhu, and R. Bamler, "Retrieval of phase history parameters from distributed scatterers in urban areas using very high resolution SAR data," *ISPRS J. Photogramm. Remote Sens.*, vol. 73, pp. 89–99, Sep. 2012. [Online]. Available: http://www.sciencedirect.com/science/article/pii/S0924271612001219

[37] C.-A. Deledalle, L. Denis, G. Poggi, F. Tupin, and L. Verdoliva, "Exploiting patch similarity for SAR image processing: The nonlocal paradigm," *IEEE Signal Process. Mag.*, vol. 31, no. 4, pp. 69–78, Jul. 2014.

[38] C. Dănişor, G. Fornaro, A. Pauciullo, D. Reale, and M. Datcu, "Super-resolution multi-look detection in SAR tomography," *Remote Sens.*, vol. 10, no. 12, p. 1894, Nov. 2018, doi: 10.3390/rs10121894.

This article has been accepted for inclusion in a future issue of this journal. Content is final as presented, with the exception of pagination.

16
IEEE TRANSACTIONS ON GEOSCIENCE AND REMOTE SENSING

[39] A. M. Tulino and S. Verdú, "Random matrix theory and wireless communications," *Found. Trends Commun. Inf. Theory*, vol. 1, no. 1, pp. 1–182, 2004, doi: 10.1561/0100000001.

[40] R. D'Agostino and M. Stephens, *Goodness-of-fit Techniques*. New York, NY, USA: Marcel Dekker, 1986.

[41] P. Kwam and B. Vidakovic, *Nonparametric Statistics With Applications to Science and Engineering*. Hoboken, NJ, USA: Wiley, 2007.

[42] W. T. V. W. H. Press, S. A. Teukolsky, and B. P. Flannery, *Numerical Recipes in C: The Art of Scientific Computing*. Cambridge, U.K.: Cambridge Univ. Press, 1988.

Simona Verde received the M.S. degree *(summa cum laude)* in telecommunication engineering and the Ph.D. degree in information engineering from the University of Naples "Parthenope," Italy, in 2011 and 2015, respectively.

Since 2011, she has been collaborating with the Institute for Electromagnetic Sensing of the Environment, National Research Council (IREA-CNR), Naples, Italy, where she is a Researcher. In 2017, she was a Visiting Scientist at the Institute of Remote Sensing and Digital Earth (RADI), Chinese Academy of Science (CAS), Bejing, China. In 2013, she also filed a patent titled "Method for Filtering of Interferometric Data Acquired by Synthetic Aperture Radar (SAR)." Her main research interests include spaceborne synthetic aperture radar (SAR) data processing, multibaseline DInSAR and SAR tomography with a special application focus on environmental and built monitoring.

Dr. Verde has been awarded at the Joint Urban Remote Sensing Event (JURSE) Student Paper Competition, São Paulo, Brazil, in 2013. She is serving as a Regular Reviewer for several journals, including the IEEE TRANSACTION ON GEOSCIENCE AND REMOTE SENSING, the IEEE GEOSCIENCE AND REMOTE SENSING LETTERS, and the IEEE JOURNAL OF SELECTED TOPICS IN APPLIED EARTH OBSERVATIONS AND REMOTE SENSING.

Antonio Pauciullo was born in Cercola, Italy, on October 10, 1969. He received the Dr.Eng. degree (Hons.) and the Ph.D. degree in information engineering from the University of Naples Federico II, Naples, Italy, in 1998 and 2003, respectively.

Since 2001, he has been with the Institute for Electromagnetic Sensing of the Environment (IREA), Italian National Research Council (CNR), Naples, where he is a Researcher, and since 2004, he has been an Adjunct Professor of digital signal processing at the University of Cassino, Cassino, Italy. His research interest is in the field of statistical signal processing with an emphasis on SAR tomography, SAR interferometry, and differential SAR interferometry.

Diego Reale (Member, IEEE) received the M.D. degree in telecommunication engineering from the University of Cassino, Cassino, Italy, in 2007, and the Ph.D. degree in information engineering from the University of Naples "Parthenope," Naples, Italy, in 2011.

Since 2007, he has been with the Institute for the Electromagnetic Sensing of the Environment, Italian National Research Council (IREA-CNR), Naples, where he is a Researcher. Since 2018, he has been teaching at the University of Naples "Parthenope". Since 2014, he has also been a Workshop Lecturer within the International Summer School on Radar/SAR organized by the Fraunhofer Institute, Bonn, Germany. In July 2016, he visited the Institute of Electronics (IE), Chinese Academy of Science (CAS), Beijing, China. In 2013, he also filed a patent titled "Method for Filtering of Interferometric Data Acquired by Synthetic Aperture Radar (SAR)." His main research interest is framed in the synthetic aperture radar (SAR) processing, with particular reference to SAR tomography, SAR interferometry, differential SAR interferometry, the development and application of SAR tomography on very high resolution SAR data for the monitoring of the built environment and critical infrastructures.

Dr. Reale's paper "Tomographic Imaging and Monitoring of Buildings with Very High Resolution Data" was awarded as the 2011 IEEE GEOSCIENCE AND REMOTE SENSING LETTER Best Paper in 2012. He has also been awarded the Second Place at the Joint Urban Remote Sensing Event 2011 Student Competition. He has also been a Session Chairman in IGARSS Conferences and also participated in the Technical Programme Committees of the IGARSS, EUSAR, and JURSE Conferences. Since 2020, he has been serving as an Associate Editor for the IEEE GEOSCIENCE AND REMOTE SENSING LETTERS.

Gianfranco Fornaro (Fellow, IEEE) received the M.S. degree *(summa cum laude)* and the Ph.D. degree in electronic engineering from the University of Naples Federico II, Naples, Italy, in 1992 and 1997, respectively.

Since 1993, he has been with IREA-CNR, Naples, Italy, where he is a Research Director working in the area of synthetic aperture radar (SAR) remote sensing. He has been an Adjunct Professor in the area of telecommunications in several universities in South Italy. In 2013, he achieved the Full Professor Habilitation in the telecommunication area. Since 2010, he has also been a Lecturer at the International Summer School on Radar/SAR organized by the Fraunhofer FHR Institute, Wachtberg, Germany; from 2013 to 2018, he was a Lecturer in the NATO Lecture Series SET 191 and SET 235.

Dr. Fornaro received the Mountbatten Premium by the IEEE Society in 1997, the 2011 IEEE GRSL Best Paper Award, and the 2011 Best Reviewers Mention of the IEEE TRANSACTIONS ON GEOSCIENCE AND REMOTE SENSING journal. He was a Guest Editor of the *EURASIP Journal on Advances in Signal Processing* and the *IEEE Signal Processing Magazine*. He is an Associate Editor of the IEEE GEOSCIENCE REMOTE SENSING LETTERS (GRSL).